Insights into BaTi1–yZryO3 ($0 \leq y \leq 1$) synthesis under supercritical fluid conditions

Gilles Philippot, Espen D. Boejesen, Catherine Elissalde, Mario Maglione, Cyril Aymonier, Bo Brummerstedt Iversen

Insights into $BaTi_{1-y}Zr_yO_3$ ($0 \leq y \leq 1$) synthesis under supercritical fluid conditions

Gilles Philippot[‡†], Espen D. Boejesen[‡], Catherine Elissalde[†], Mario Maglione[†], Cyril Aymonier[†*] and Bo B. Iversen[‡**]

[‡]Center for Materials Crystallography, Department of Chemistry and iNANO, Aarhus University, Aarhus, Denmark

[†]CNRS, Univ. Bordeaux, ICMCB, UPR 9048, F-33600 Pessac, France

ABSTRACT: The production of $BaTi_{1-y}Zr_yO_3$ ($0 \leq y \leq 1$, BTZ) nanocrystals is known to be challenging due the low reactivity of zirconium precursors. Here we have successfully studied the zirconium impact on the BTZ particles formation in sub- and supercritical fluid conditions along the entire solid solution. *In situ* synchrotron wide angle X-ray scattering (WAXS) analyses were conducted in batch at 150°C and 400°C to follow in real time the BTZ crystallites synthesis. This revealed the complexity underneath the nucleation and growth mechanisms of ABO_3 nanocrystals, especially going towards high zirconium content (more than 50 atomic %). This type of substitution induces, among other things, microstrain within the structure. Moreover, for $BaTi_{0.4}Zr_{0.6}O_3$ and $BaTi_{0.2}Zr_{0.8}O_3$ cases, the experiments showed the apparition of two crystallite size populations. In the $BaTi_{0.4}Zr_{0.6}O_3$ case, at 400°C, these two size populations merged in a single one after at least eight minutes but not in the $BaTi_{0.2}Zr_{0.8}O_3$ one. The zirconium content being higher, the particles become more refractory, thus, the temperature is not high enough to enable their ripening. It is important to note that this behavior was not observed for particles produced at 400°C but in flow, with a residence time of only 50 s. There, the particles presented a single size population, close to the one obtained after eight minutes in batch. Meaning that, for batch syntheses, a longer time is required to achieve a similar product quality to the one obtained with a flow process.

1. INTRODUCTION

Perovskite oxide materials are largely used in passive electronic components, such as capacitors, actuators, resonators, etc. Consequently, these electroceramics, with enhanced ferro-piezoelectric properties, are a centerpiece of current electronic devices and still present major challenges. Indeed an improved control of the perovskite oxide nanoparticle syntheses, such as composition and microstructure, has to be tackled to fit into the current environmental and integrated strategies.[1–7] The remarkable ability to tune the properties of lead free materials belonging to the $BaTi_{1-y}Zr_yO_3$ (with $0 \leq y \leq 1$, BTZ) solid solution has focused great attention for both applied and fundamental researches. These compounds are attractive candidates as tunable capacitors (low leakage current, high breakdown field strength) and exhibit promising potentialities as high strain materials.[8–10] BTZ ceramics present versatile dielectric behavior, changing from classical ferroelectric when $y \leq 0.15$, over a diffuse phase transition when $0.15 \leq y \leq 0.30$ to relaxor behavior when $y \geq 0.30$ simply by adjustment of the Zr to Ti ratio.[11–22] Such gradual cross-over from ferroelectric to relaxor state is driven by the Zr concentration. Increasing Zr/Ti ratio induces polar disorder at the origin of the specific relaxor behavior. The corresponding merging of phase transitions leads to a high polarization flexibility that is expected to contribute to the strain level. The zirconium content influences also the microstructure in terms of grain size, affecting thus the transitions temperatures, the permittivity values and the domain configuration.[23] The structural phase diagram of the system $BaTiO_3$ - $BaZrO_3$ (BT - BZ) system depends on the control of composition underlying thus the obvious key role of zirconium on chemical reactivity and homogeneity. In particular, in the high substitution regime, stiffest synthesis conditions are required and the reliability of the functional properties strongly depends on the control of the materials chemistry.

So far, one of the most suitable ways of producing the complete solid solution is the solid state one. Nevertheless, due to the low Zr reactivity, very high synthesis temperatures are required (1200 °C) and despite this, the powders can still exhibit a lack of homogeneity, especially in the $BaZrO_3$–rich region.[19–21] In an effort to improve the control of BTZ synthesis, we have recently reported the fast, scalable and reliable supercritical flow synthesis of well crystalized BTZ nanocrystals along the entire solid-solution range.[24] This synthesis method addresses the requirements of a major challenge for size reduction and increased packing tendency, allowing the development of a feasible large scale production of high quality nanocrystals with tunable stoichiometry, using soft synthesis conditions. [25–35] We have also shown in our work that the as-obtained nanoparticles can be successfully densified using Spark Plasma Sintering (SPS).[36] Dielectric characterization performed on high density nanostructured ceramics (grain size < 100nm) revealed the so called “size effect” on the local structure coherence and consequently on the macroscopic dielectric

properties.[6,36–44] Another interesting finding of that particular study,[36] was the establishment of a correlation between the composition and final size of the particles. In an effort to improve the control of the synthesis over the final grain size and, as a result the dielectric properties, additional research efforts must be focused on the understanding of the formation and growth mechanisms governing the nanocrystal synthesis under supercritical fluid conditions. Reaching such higher level of synthesis control is a key challenge to increase the potentiality of lead free materials in the field of electronics.

To answer to this fundamental question we combined *in situ* with *ex situ* experiments while screening the entire BTZ solid solution. Indeed, the use of *in situ* measurements has already been proven to be a true asset in the understanding of barium titanate based nanomaterials formation under hydro- and solvothermal condition. [45–49] Here, *in situ* synchrotron wide angle X-ray scattering (WAXS) studies of nanocrystals formation in sub- and supercritical fluid batch conditions were performed for low (y = 0.15 and 0.30) and high (y = 0.60 and 0.80) zirconium content. The specific compositions y = 0.15 and 0.30 were chosen in order to investigate a potential effect of the material property transition, from ferroelectric to relaxor, on the crystallite growth. The case of y = 0.6 and 0.8 are "extreme" cases chosen to study the zirconium impact at high content. It is important to note that for technological issues, it is not possible to mimic the flow synthesis for *in situ* measurements. In parallel, conventional *ex situ* X-ray powder diffraction (XRD), transmission electron microscopy (TEM), scanning transmission electron microscopy (STEM) analyses were conducted on powders produced in supercritical flow conditions to support the *in situ* observations. The supercritical fluid synthesis of BTZ nanocrystals, was screened along a linear range of compositions, ensuring a representative broad screening of the solid solution (y = 0 , 0.2, 0.4, 0.6, 0.8 and 1), the specific cases of y = 0.15 and 0.30 were discussed in our previous study *for ex situ*.[24]

2. MATERIALS AND METHODS

2.1. Materials

The precursor chemicals used were barium isopropoxide, zirconium isopropoxide, titanium isopropoxide and absolute ethanol. All chemicals were of 99.9% purity and used as received from Sigma Aldrich.

2.2. Nanocrystal synthesis and characterization

The BTZ syntheses were carried out using two different setups: 1) a flow synthesis apparatus with a potential of a large scale synthesis,[50–58] and 2) a batch *in situ* setup making it possible to follow in real time the formation of the material at the given synthesis conditions.[59–65]

2.2.1 *In situ* experiments. The WAXS study was carried out at beamline i711 at MAXII, MAX-lab, Lund, Sweden.[66] The alkoxide precursors were first dissolved in ethanol for 30 minutes and subsequently mixed with water to match an ethanol-water molar ratio of 0.29, as defined in previous studies,[49,67–71] to form gels. These gels were prepared with precursors concentrations ranging from 0.04 up to 0.5 $mol.L^{-1}$. The respective precursor mixtures were subsequently injected into sapphire capillaries with an inner diameter of 0.7 mm and outer diameter of 1.1 mm. The filled capillary was connected to a HPLC pump via Swagelok© fittings and graphite ferrules and pressurized to 23 MPa. Heating was applied with temperatures of either 150 or 400°C to initiate the reaction by remotely switching a preheated jet of hot air as described elsewhere.[62] The reaction was followed by shining a 12.3 keV X-ray beam ($\lambda \approx 1$ Å) on the capillary and the scattered radiation was continuously collected on a 2 dimensional CCD detector (Oxford). The time resolution of the experiments was 5 s and each synthesis was followed for a period of 8 minutes.

2.2.2. *In situ* data analysis. The two dimensional powder X-ray scattering patterns were integrated into a one dimension pattern using Fit2D software.[72] The parameters needed for proper integration, i.e., sample to detector distance, detector tilt, detector rotation and beam center, were obtained from calibration using a NIST SRM 660B LaB_6 standard sample. Sequential Rietveld refinements were conducted using the Fullprof software suite.[73] The data were fitted in the region of 10-41° 2θ using at least an 8th order Chebychev polynomial for background modelling. The $BaTiO_3$ sample was fitted using the tetragonal P4mm structure, while the data from samples with other compositions were fitted in the space group $Pm\bar{3}m$ due to the almost cubic nature of the $BaTiO_3$ cell (unit cell parameters = 3.999 Å, 3.999 Å and 4.018 Å— according to ICSD card #67 520), the nanosize of the particles and the limited resolution of the used instrument. The nanosized dimensions of the crystallites broadened the Bragg peaks, removing the minute peak splitting ((200) and (002)) occurring due to the tetragonal symmetry. The refined parameters include scale factor, unit cell parameters, Gaussian and Lorentzian size broadening contributions (I_G, X and Y), isotropic atomic displacement parameters for titanium and zirconium and the instrumental zero point.[73] The profile function used for fitting the patterns is the implemented Thompson – Cox – Hasting formulation of the pseudo-Voigt function in the Fullprof software suite.[74] The instrumental contribution to the peak profiles was accounted for implementing the instrumental resolution function obtained from a refinement of the diffraction data collected form the NIST LaB_6 sample. The profile widths (full width half max) corrected for the instrumental resolution were used to calculate the particle size based on the Scherrer equation (see ESI),[75–77] and in some cases also to determine the isotropic microstrain contribution as defined by Stokes and Wilson and implemented in the Fullprof software suite.[78]

2.3. *Ex situ* experiments

The flow synthesis setup used in this study is described in greater details elsewhere.[24,49] It consists of two injection lines which meet and their contents are mixed at the inlet of the synthesis reactor set at 400°C and 23 MPa. One line is kept at room temperature and 23 MPa to inject the ethanolic precursors solutions with a concentration of $3 \cdot 10^{-2}$ M. The second injection line is dedicated to feeding the reactor with preheated water at a temperature of 150°C and

pressure of 23 MPa. By doing so the high heating rates needed for quickly achieving the set-point temperature of 400°C are easily realizable. The synthesis reactor itself is a 24 meters tubular reactor (1/8" inch in diameter) and the residence time of each reaction is estimated to be around 50 seconds with an overall pressure set at 23 MPa. By doing so the high heating rates needed for quickly achieving the set-point temperature of 400°C are easily realizable. The synthesis reactor itself is a 24 meters tubular reactor (1/8" inch in diameter) and the residence time of each reaction is estimated to be around 50 seconds with an overall pressure set at 23 MPa. Based on the paper by Bazaev et al. and an assumed ethanol/water ratio of 0.29, the critical point was estimated to be T_c= 305 °C and $13 \leq P_c \leq 17$ MPa.[79] Thus the reactions were conducted at supercritical fluid conditions (T= 400°C and P= 23 MPa).

X-ray diffraction (XRD) patterns were collected on a PANalytical Bragg-Brentano θ-2θ geometry diffractometer equipped with a secondary monochromator over an angular range of 2θ = 5-120° with a step of 0.02°. The Cu-K_α radiation was generated at 45 kV and 40 mA (λ = 0.15418 nm).

Elemental analysis was performed with an inductively coupled plasma (ICP) apparatus ICP-OES 720ES from Varian.

High-resolution transmission electron microscopy (HR-TEM) and high resolution scanning electron microscopy (HR-STEM) images were collected on a TALOS F200A with a TWIN lens system, a field emission gun (FEG) type X-FEG as electron source and a Ceta 16M Camera. A Super-X EDS Detector was used for spatially resolved elemental analysis, with a spatial resolution of approximately 2 nm, using the same TALOS microscope in STEM mode and the Bruker Esprit software. Exposure times of 7 minutes were used to create elemental distribution maps with satisfactory counting statistics. This approach minimizes potential problems related to beam damage and specimen drift. STEM pictures were obtained using a High Angle Annular Dark Field detector (HAADF).

3. RESULTS AND DISCUSSION

In an effort to improve our understanding regarding the BTZ nanoparticles formation (see ESI Table T1 for ICP results) and especially their size variation according to the zirconium content as shown in Figure 1 and ESI Figure S1,[24] *in situ* synchrotron WAXS studies of the system were performed.

The possibility to track, in real time, the crystallite formation. In the present study, BTZ compounds with compositions of y = 0, 0.15, 0.3, 0.6, 0.8 have been investigated. Note that the standard deviations of the refined sizes in all cases are on the order of the symbols used in the plots and are thus omitted for clarity.

Figure 2a shows the crystallite size variation as a function of time for three compositions, in the range of $0 \leq y \leq 0.3$, synthesized at 400°C with a precursor concentration of 0.2 M. The curves reveal that with increasing Zr content there is a decrease in absolute crystal size after 8 min, as well as a significant decrease in the amount of relative crystal growth. Indeed, the crystallite size for y = 0.3 after 8 min of reaction is almost the same as after only 0.1 min of reaction.. This effect appears in particular at the earliest stage of the synthesis which is heavily influenced by the zirconium content. An increased Zr content limits the growth and favors the nucleation. This behavior is similar to the observed effect of increasing overall precursor concentration while retaining a constant composition of $BaTiO_3$ (Figure 2b). Increasing the precursor concentration from 0.04 to 0.5 mol.L^{-1} decreases the overall amount of particle growth and increases the growth kinetics. The trend may be rationalized on the basis of the nucleation and growth theory developed by LaMer and Dinegar.[80,81] During nucleation the amount of precursor available for nucleation and growth decreases. At a low starting concentration, e.g., 0.04 M, the minimum concentration condition for nucleation is quickly no longer present and as a consequence the nucleation will stop and instead growth will occur. The growth process thus consumes the remaining precursor in solution by increasing the average crystallite size via various growth mechanisms. For high precursor concentrations nucleation plays a greater role and will occur on a timescale much faster than any simultaneous growth. The almost "burst nucleation" like behavior will bring about a depletion of the precursor left in solution for growth, which accordingly will only occur to a very limited degree. Consequently, as a function of increasing precursor concentration there is a decrease in absolute crystal size observed after 8 min, e.g., as it is the case for the experiments performed for the BT system between 0.04 and 0.5 M shown here.. For the case of intermediate concentrations, e.g., 0.2 M an equilibrium between the two mechanisms is established and both nucleation and growth occur simultaneously followed by a complete halt of nucleation, albeit with continued growth. Comparing these observations and explanations with the trends observed in the case of varying Zr concentration, it may be proposed that the minimum concentration for burst nucleation decreases with increasing Zr content and nucleation is simply dominating at high Zr contents. This is supported when comparing the normalized crystallite size and scale factor variations with time (see ESI Figure S2). The variation of the normalized scale factor, which is proportional to the volume of coherently scattering material, shows a similar evolution upon changing the Zr content. Thus, the evolution and overall proportion of crystallized material is the same in each three experiments. However, as already mentioned, with increasing Zr content, there is a decrease in absolute crystal size, as well as a significant decrease in the amount of relative crystal growth. This is in agreement with the proposed burst nucleation mechanism where a larger number of nuclei are quickly formed but do not grow due to lack of precursor available for growth. Moreover, with time, the normalized scale factor variation follows the normalized crystallite size in all cases. Therefore, the crystallites grow through precursor condensation and not ripening. If the growth was due to ripening, the overall quantity of crystallized material and thus, the scale factor, would be constant, while the crystallites size simultaneously would increase. Indeed, the nucleation may very well be dependent on the presence of particular pre-nucleation structures which

could be highly influenced by the Zr content in solution. In previous studies of oxide synthesis under hydro-and solvothermal conditions it has been shown that various pre-nucleation structures play a vital role in directing the nucleation and growth.[60,63] This directing influence is not only limited to the size evolution but also to the preferred formation of one crystalline polymorph over another.

The *in situ* study conducted for the compounds with compositions y = 0.6 and 0.8 revealed an interesting behavior during particle growth illustrated in Figure 3. The figure shows a number of XRD patterns collected after 10 s, 50 s, 5 min and 8 min of reaction time superimposed on each other. The patterns are for the syntheses of $BaTi_{0.4}Zr_{0.6}O_3$ performed at 400 and 150°C, respectively (see ESI Figure S3 for $BaTi_{0.2}Zr_{0.8}O_3$ experiment). An overall shift of the Bragg peak positions towards higher scattering angles, i.e., smaller unit cells, with time is observed. This indicates a more dense structure and may be due to a decrease in structural defects or other similar effects that may help relax the structure. At 400°C, a clear splitting, increasing with scattering angle, is observed for all peaks (Figure 3c) at the beginning of the synthesis (10 s). However, over time this splitting progressively weakens and finally disappears. In the case of a synthesis temperature of 150 °C (Figure 3d) the splitting does not disappear with prolonged synthesis time.

Based on these observations we propose two possible scenarios as the cause of the observed peak splitting: i) at the beginning of the synthesis Ti / Zr inhomogeneity exists in the pre-nucleation structures and as a consequence, two groups of distinctly different nanoparticles initially form. One group of crystals is Ti-rich and the other Zr-rich. This arrangement would bring about two groups of crystallites with significantly differing lattice parameters and accordingly produce a peak splitting in the XRD pattern. The disappearance of the splitting in this case is explained by a temperature dependent homogenization of the overall elemental distribution in the particles. Another explanation is ii) that initially two groups of nanocrystals with the same composition but with distinctly different size distributions around two different mean values exist. The peak splitting in this case is assumed to be a consequence of changes in the lattice parameters due to size dependent changes in surface strain. With time, ripening causes a homogenization of particles, producing particles with crystallite sizes grouped around one single mean value and lattice parameter. In both suggested cases, i.e., i) and ii), it is safe to say that at a temperature of 150 °C the energy does simply not suffice to ensure a complete homogenization or ripening, respectively.

To investigate in greater details which of the two hypotheses might be the correct one *ex situ* XRD patterns of the supercritical flow synthesized samples were re-investigated. Additional refinement parameters were included compared to the results presented in the previous publication on the results of the flow synthesis.[24] The background was modeled using a Chebyshev polynomial function instead of using a linear interpolation between data points. Moreover test refinements including two groups of crystallites of differing sizes and unit cell parameters were conducted, however, refinements based on this model did note improve the fits significantly. As an alternative an isotropic microstrain parameter, corresponding to 1/4 of the apparent microstrain defined by Stokes and Wilson,[78,82] was introduced. Including this microstrain parameter improved the overall refinement quality; an effect highlighted in Table 1, which lists all the R_B-factors, R_F-factors and χ^2 values (these values show how well the refined model fits with the experimental PXRD data). In particular the fits in the Zr rich region of the BTZ solid solution ($0.4 \leq y \leq 0.8$) were improved significantly (see ESI Table T2).

The magnitude of the refined microstrain changes significantly upon variation in Zr composition. Figure 4 presents the microstrain variation as function of zirconium content. When y = 0 or 1, the microstrain remains low, which is not surprising since the refinement quality presented in Table 1 did not change much. However, increasing the Zr content from y = 0.2 up to y = 0.8 drastically impacted the microstrain value which first increased then decreased upon further addition of Zr to go back almost to zero when y =1. The trend can be understood from a structural point of view. The zirconium (IV) cationic radius is bigger than the titanium (IV) radius (r_{Zr} = 0.86 Å and r_{Ti} = 0.75 Å), accordingly increasing the zirconium amount will increase the average unit cell parameter.[83] The microstrain being intimately related to the distribution of unit cell parameters present in each crystallite, a broad distribution of possible unit cell parameters will lead to a large degree of microstrain.[84] The non-zero microstrain of the $BaTiO_3$ and the 0.2 doped sample may be reflecting the presence of a mixture of cubic and tetragonal $BaTiO_3$ phase, a phenomenon previously reported to be present in nanosized samples of this compound.[28,29,36,37,39,41,85] This also serves to explain why there is a larger microstrain for the pure $BaTiO_3$ sample than for the pure $BaZrO_3$ sample, since in the latter no core shell structure is known to form. It is also interesting to note that this microstrain appears to be the highest for a composition range where the material presents a piezoelectric behavior.

With the data at hand it is not possible to choose one hypothesis over the other to explain the peaks splitting: i) Ti / Zr inhomogeneities or ii) two size populations. However, the *ex situ* XRD data and STEM-EDX analysis of the flow synthesized powders does not suggest the presences of stoichiometric inhomogeneities for any of the investigated samples as Figure 5 illustrates it with the $BaTi_{0.8}Zr_{0.2}O_3$ case. That is why, in the following, we have chosen to describe the observed trends within the framework of hypothesis ii), i.e., the splitting is caused by groups of crystallites with different sizes, same average composition and different unit cell parameters caused by size related effects and furthermore to include an isotropic microstrain contribution. This being said the interpretation provided may easily be altered somewhat to incorporate compositional differences between the two groups. In Figure 6 Rietveld refinement fits of *in situ* XRD patterns collected at different points in time during the $BaTi_{0.4}Zr_{0.6}O_3$

synthesis performed at 400°C are presented. There, Ycalc is the intensity of the PXRD calculated and Yobs: intensity of the measured PXRD. The figure highlights how the incorporation of another BTZ phase enables the possibility of a proper fit during the entire course of synthesis. At the earlier stage of synthesis (10 s) the Bragg positions of the two phases are distinctly different. With time this difference decreases continuously (50 s and 5 min) and after 8 minutes the difference is minute. The XRD pattern obtained after 8 minutes of synthesis can similarly be fitted satisfactorily by including an isotropic microstrain contribution but only one BTZ phase (Figure 7), resembling to the results obtained from the *ex situ* synthesis (see ESI Figure S4)

In Figure 8 the extracted crystallite sizes for both "groups": the BTZ phases with the same stoichiometry but differing sizes and unit cell parameters, of $BaTi_{0.4}Zr_{0.6}O_3$ and $BaTi_{0.2}Zr_{0.8}O_3$ produced at 150°C and 400°C, respectively are plotted as a function of time. In the case of $BaTi_{0.4}Zr_{0.6}O_3$ at 400°C (Figure 8a), the so called "group 2" has a constant crystallite size of around 19 - 20 nm which is reached almost immediately upon heating. The other one (group 1) presents a two-stage formation and growth mechanism; assuming the nucleation and growth can be described by classical models. During the first two minutes the growth curve of group 1 follows a curve commonly observed for conventional sol–gel-like nucleation and growth mechanisms. After approximately 2 min ripening starts to be the dominating factor (Figure 8a) and accordingly brings about the single group of particles observed at the final stage of synthesis. The same synthesis was carried out at a lower temperature, i .e, 150°C (Figure 8b). Similarly two distinct groups of particles are observed. The particles in the group 2, with larger sizes, have a constant average crystallite size of around 16- 17 nm. The particles of group 1 start out small (11 – 12 nm) and initially follows a similar nucleation and growth behavior to the one observed in the case of group 1 shown in Figure 8a. However, in this case (150°C), the secondary growth due to ripening does not occur and even after 8 min two distinctly different groups of particles exist. Assuming the classical growth models are valid the simple explanation for this difference is the lack of energy available for ripening of the group of sub 20 nm nanocrystals.

Support of the suggested explanation is provided by plotting the normalized scale factor alongside the normalized crystallite size as function of time for the group 1 crystallites of $BaTi_{0.4}Zr_{0.6}O_3$ synthesis at 400°C (Figure 9). The scale factor quickly reaches a more or less constant value, however, at the same time the crystallite size continuously increases. Since the scale factor is proportional to the volume of coherently scattering material this behavior indicates that no additional crystalline material is formed while the particles are growing, i.e., Ostwald ripening occurs. The crystallite sizes of the two respective groups for the composition $BaTi_{0.2}Zr_{0.8}O_3$ are shown in Figure 8c and d for 400 °C and 150 °C, respectively. Similar behavior, as observed for the case of $BaTi_{0.4}Zr_{0.6}O_3$, is initially observed. At 400°C (Figure 8c) one group with a constant crystallite size around 19 - 20 nm exists together with a second group having a smaller crystallite size. Until around two minutes the growth of the second group may be described as following a nucleation and growth type behavior. The growth and subsequent ripening is, however, not as pronounced as it was the case for the $BaTi_{0.4}Zr_{0.6}O_3$. One possible explanation for this difference may be related to the Zr content. An increase in Zr content in the precursor mixture leads to a lower critical concentration for nucleation to occur due to changes in solubility and a consequence supersaturation. An effect of these combined changes is that burst nucleation of nanocrystals with smaller sizes (ca. 16 nm) happens initially; depleting the amount of precursor left for additional nucleation and growth. Subsequent ripening only occurs to a very limited degree. It thus appears that Zr not only lowers the nucleation barrier but, furthermore, hinders ripening.

One explanation may be that the Zr cation reactivity is lower than the Ti cation,[86] the temperature of 400°C is simply insufficient for significant ripening to occur. At 150°C even less ripening occurs due to a combination of high Zr content and low temperatures, nevertheless, the temperature is sufficient for burst nucleation to occur. This low temperature process produces two groups of particles with almost constant sizes of 18 nm and 9.5 nm, respectively. The significant differences between the results from the *ex situ* and *in situ* studies, e.g., the lack of any bi modal size distribution in the *ex situ* data, may be explained by significant differences in the synthesis procedures. In particular the hydrolysis step occurs over different time-scales for the *in situ* and flow syntheses respectively. In the flow synthesis the precursors are mixed in a flow type manner at elevated temperatures, i.e., the mixing occurs within a few seconds and above room temperature (water line preheated at 150 °C). In stark contrast hereto the precursors are mixed several minutes ahead of the heating in the *in situ* study and the mixing occurs at ambient conditions. As a consequence great differences in size, composition and structure of any initially formed pre-nucleation clusters may exist. The presence of pre-nucleation clusters also may serve to explain the large size of the initial crystallites formed, as has previously been shown to happen in other oxide systems during solvothermal conditions.[60,63,87]

CONCLUSION

In this work we show the complexity underlying the ABO_3 nanocrystals formation and growth mechanisms in sub- and supercritical fluid conditions. This, especially when using precursors containing low reactivity elements such as Zr. Indeed, it is the Zr content which directly impacts the nanocrystals growth especially in the Zr rich domain of the BTZ solid solution. There, a microstrain contribution has to be incorporated to obtain the optimal model for an accurate description of the observed PXRD data.

Moreover, combining *in situ* WAXS analyses of BTZ batch syntheses with *ex situ* characterizations of BTZ powders produced in flow highlighted two different trends; i) at low Zr content (< 50%), both setups enable the produc-

tion of similar products in terms of crystallite size regarding synthesis duration. However, ii) when producing BTZ with high Zr content, the batch process will yield two particle size distributions which can ultimately merge through ripening after several minutes (> 8 minutes) if the temperature is high enough regarding the Zr/Ti ratio. On the contrary, for the flow syntheses, even if the residence time in the reactor is only around 50 s, a single size population is observed, similar to the one obtained after 8 minutes in batch.

To conclude, the supercritical flow process appears to be an excellent method for achieving a pristine product with a monodisperse size distribution within a timeframe of less than a minute regardless to the Zr content while a batch type process, e.g., the method used for *in situ* synthesis, requires at least 8 minutes of heating to achieve a similar product quality. In the latter case, pre-nucleation clusters appearing during the cold mixing of the precursors might be responsible for this difference. Thus, to understand the full story behind BTZ nanocrystals growth it is necessary to combine *in situ* total X-ray scattering experiments with pair distribution function analysis. This ongoing study will provide more details on the atomic arrangement in the amorphous precursor mixture used as well as unravel the presence of any possible intermediate amorphous phases or growth units.

ASSOCIATED CONTENT

Supporting Information. Additional information i) on the elemental analysis of the BTZ powders produced in flow and on the crystallite size calculations based on the PXRD refinements, ii) TEM pictures of the BTZ nanocrystals, iii) Representative original WAXS spectra of $BaTiO_3$ nanocrystals formation with time, iv) variation of the normalized crystallite size and normalized scale factor with time for y = 0; 0.15 and 0.3, v) variation of the WAXS patterns ($\lambda \approx 0.99361$ Å) during the synthesis of $BaTi_{0.2}Zr_{0.8}O_3$ crystallites at different synthesis temperatures: 400°C and 150°C with a zoom around 39°, vi).on the impact of using the microstrain parameter on PXRD fits of powders produced in flow and vii) on the interest of using a two phase refinement for *in situ* experiments, especially in the Ti rich region, are presented. This material is available free of charge via the Internet at http://pubs.acs.org.

AUTHOR INFORMATION

Corresponding Authors

* Dr. Cyril Aymonier
e-mail: cyril.aymonier@icmcb.cnrs.fr

** Prof. Bo Iversen
e-mail: bo@chem.au.dk

Author Contributions

All authors have given approval to the final version of the manuscript.

ACKNOWLEDGMENT

The authors acknowledge the IDS FunMat European doctoral school, the Region Aquitaine and the Danish National Research Foundation, the project DNRF93 and the Innovations Fonden (4107-00008B-GCAM) for their financial support.

REFERENCES

(1) Ravez, J.; Simon, A. Perovskite Relaxor Ferroelectrics Free from Lead. *J. Korean Phys. Soc.* **1998**, *32* (3 SUPPL.), S955–S956.

(2) Villafuerte-Castrejón, M.; Morán, E.; Reyes-Montero, A.; Vivar-Ocampo, R.; Peña-Jiménez, J.-A.; Rea-López, S.-O.; Pardo, L. Towards Lead-Free Piezoceramics: Facing a Synthesis Challenge. *Materials (Basel).* **2016**, *9*, 21.

(3) Fridkin, V.; Ducharme, S. *Ferroelectricity at the Nanoscale: Basics and Applications*, Springer.; Verlag Berlin Heidelberg, 2014.

(4) Rohrer, G. S.; Affatigato, M.; Backhaus, M.; Bordia, R. K.; Chan, H. M.; Curtarolo, S.; Demkov, A.; Eckstein, J. N.; Faber, K. T.; Garay, J. E.; Gogotsi, Y.; Huang, L.; Jones, L. E.; Kalinin, S. V.; Lad, R. J.; Levi, C. G.; Levy, J.; Maria, J.-P.; Mattos, L.; Navrotsky, A.; Orlovskaya, N.; Pantano, C.; Stebbins, J. F.; Sudarshan, T. S.; Tani, T.; Scott Weil, K. Challenges in Ceramic Science: A Report from the Workshop on Emerging Research Areas in Ceramic Science. *J. Am. Ceram. Soc.* **2012**, *95*, 3699–3712.

(5) Zhang, S.; Li, F.; Jiang, X.; Kim, J.; Luo, J.; Geng, X. Advantages and Challenges of Relaxor-$PbTiO_3$ Ferroelectric Crystals for Electroacoustic Transducers-A Review. *Prog. Mater. Sci.* **2015**, *68*, 1–66.

(6) Zhao, Z.; Buscaglia, V.; Viviani, M.; Buscaglia, M.; Mitoseriu, L.; Testino, A.; Nygren, M.; Johnsson, M.; Nanni, P. Grain-Size Effects on the Ferroelectric Behavior of Dense Nanocrystalline $BaTiO_3$ Ceramics. *Phys. Rev. B* **2004**, *70*, 024107.

(7) Koziej, D.; Lauria, A.; Niederberger, M. 25th Anniversary Article: Metal Oxide Particles in Materials Science: Addressing All Length Scales. *Adv. Mater.* **2014**, *26*, 235–257.

(8) Buscaglia, V.; Tripathi, S.; Petkov, V.; Dapiaggi, M.; Deluca, M.; Gajović, A.; Ren, Y. Average and Local Atomic-Scale Structure in $BaZr_xTi_{1-x}O_3$ (x = 0. 10, 0.20, 0.40) Ceramics by High-Energy X-Ray Diffraction and Raman Spectroscopy. *J. Phys. Condens. Matter* **2014**, *26*, 065901.

(9) Maiti, T.; Guo, R.; Bhalla, A. S. Structure-Property Phase Diagram of $BaZr_xTi_{1-x}O_3$ System. *J. Am. Ceram. Soc.* **2008**, *91*, 1769–1780.

(10) Laulhé, C.; Hippert, F.; Kreisel, J.; Maglione, M.; Simon, A.; Hazemann, J. L.; Nassif, V. EXAFS Study of Lead-Free Relaxor Ferroelectric $BaTi_{1-x}Zr_xO_3$ at the Zr K Edge. *Phys. Rev. B* **2006**, *74*, 014106.

(11) Bera, J.; Rout, S. K. On the Formation Mechanism of $BaTiO_3$–$BaZrO_3$ Solid Solution through Solid-Oxide Reaction. *Mater. Lett.* **2005**, *59*, 135–138.

(12) Jeong, I.-K.; Park, C. Y.; Ahn, J. S.; Park, S.; Kim, D. J. Ferroelectric-Relaxor Crossover in $BaTi_{1-x}Zr_xO_3$ Studied Using Neutron Total Scattering Measurements and Reverse Monte Carlo Modeling. *Phys. Rev. B* **2010**, *81*, 214119.

(13) Kajtoch, C. Influence of Zr-Substitution on Phase Transitions Character in Polycrystalline $BaTi_{1-x}Zr_xO_3$. *J. Mater. Sci.* **2010**, *46*, 1469–1473.

(14) Maiti, T.; Guo, R.; Bhalla, A. S. Evaluation of Experimental Resume of $BaZr_xTi_{1-x}O_3$ with Perspective to Ferroelectric Relaxor Family: An Overview. *Ferroelectrics* **2011**, *425*, 4–26.

(15) Miao, S.; Pokorny, J.; Pasha, U. M.; Thakur, O. P.; Sinclair, D. C.; Reaney, I. M. Polar Order and Diffuse Scatter in $BaTi_{1-x}Zr_xO_3$ Ceramics. *J. Appl. Phys.* **2009**, *106*, 114111.

(16) Rabuffetti, F. a.; Brutchey, R. L. Complex Perovskite Oxide Nanocrystals: Low-Temperature Synthesis and Crystal Structure. *Dalton Trans.* **2014**, *43*, 14499–14513.

(17) Rabuffetti, F. a.; Brutchey, R. L. Local Structural Distortion of $BaZr_xTi_{1-x}O_3$ Nanocrystals Synthesized at Room Temperature. *Chem. Commun.* **2012**, *48*, 1437–1439.

(18) Simon, A.; Ravez, J.; Maglione, M. The Crossover from a Ferroelectric to a Relaxor State in Lead-Free Solid Solutions. *J. Phys. Condens. Matter* **2004**, *16*, 963–970.

(19) Maiti, T.; Alberta, E.; Guo, R.; Bhalla, a. S. The Polar Cluster like Behavior in Ti^{4+} Substituted $BaZrO_3$ Ceramics. *Mater. Lett.* **2006**, *60*, 3861–3865.

(20) Maiti, T.; Guo, R.; Bhalla, a. S. The Evolution of Relaxor Behavior in Ti^{4+} Doped $BaZrO_3$ Ceramics. *J. Appl. Phys.* **2006**, *100*, 114109.

(21) Nuzhnyy, D.; Petzelt, J.; Savinov, M.; Ostapchuk, T.; Bovtun, V.; Kempa, M.; Hlinka, J.; Buscaglia, V.; Buscaglia, M. T.; Nanni, P. Broadband Dielectric Response of $Ba(Zr,Ti)O_3$ Ceramics: From Incipient via Relaxor and Diffuse up to Classical Ferroelectric Behavior. *Phys. Rev. B* **2012**, *86*, 014106.

(22) Halder, S.; Schneller, T.; Böttger, U.; Waser, R. Fabrication and Electrical Characterisation of Zr-Substituted $BaTiO_3$ Thin Films. *Appl. Phys. A* **2004**, *81*, 25–29.

(23) Curecheriu, L. P.; Frunza, R.; Ianculescu, A. Dielectric Properties of the $BaTi_{0.85}Zr_{0.15}O_3$ Ceramics Prepared by Different Techniques. *Process. Appl. Ceram.* **2008**, *2*, 81–88.

(24) Philippot, G.; Albino, M.; Chung, U.-C.; Josse, M.; Elissalde, C.; Maglione, M.; Aymonier, C. Continuous $BaTi_{1-y}Zr_yO_3$ ($0 \le y \le 1$) Nanocrystals Synthesis in Supercritical Fluids for Nanostructured Lead-Free Ferroelectric Ceramics. *Mater. Des.* **2015**, *86*, 354–360.

(25) Huang, L.; Chen, Z.; Wilson, J. D.; Banerjee, S.; Robinson, R. D.; Herman, I. P.; Laibowitz, R.; O'Brien, S. Barium Titanate Nanocrystals and Nanocrystal Thin Films: Synthesis, Ferroelectricity, and Dielectric Properties. *J. Appl. Phys.* **2006**, *100*, 034316 1–10.

(26) Maglione, M.; Philippot, G.; Levasseur, D.; Payan, S.; Aymonier, C.; Elissalde, C. Defect Chemistry in Ferroelectric Perovskites: Long Standing Issues and Recent Advances. *Dalt. Trans.* **2015**, *44*, 13411–13418.

(27) Petkov, V.; Buscaglia, V.; Buscaglia, M.; Zhao, Z.; Ren, Y. Structural Coherence and Ferroelectricity Decay in Submicron- and Nano-Sized Perovskites. *Phys. Rev. B* **2008**, *78*, 054107.

(28) Philippot, G.; Elissalde, C.; Maglione, M.; Aymonier, C. Supercritical Fluid Technology: A Reliable Process for High Quality $BaTiO_3$ Based Nanomaterials. *Adv. Powder Technol.* **2014**, *25*, 1415–1429.

(29) Wada, S.; Hoshina, T.; Takizawa, K.; Ohishi, M.; Yasuno, H.; Kakemoto, H.; Tsurumi, T.; Moriyoshi, C.; Kuroiwa, Y. Origin of Ultrahigh Dielectric Constants for Barium Titanate Nanoparticles. *J. Korean Phys. Soc.* **2007**, *51*, 878.

(30) Zhang, Y.; Wang, X.; Kim, J.; Kim, J.-R.; Hur, K.-H.; Li, L. Uniform Coating of $BaTiO_3$ -Dy_2O_3 - SiO_2 Compound Nano Layer on Ni Particles for MLCC Electrode. *J. Am. Ceram. Soc.* **2013**, *96*, 2163–2166.

(31) Zhang, Y.; Wang, X.; Tian, Z.; Hur, K.-H.; Li, L. Preparation of BME MLCC Powders by Aqueous Chemical Coating Method. *J. Am. Ceram. Soc.* **2011**, *94*, 3286–3290.

(32) Zhu, X.; Wang, J.; Zhang, Z.; Zhu, J.; Zhou, S.; Liu, Z.; Ming, N. Atomic-Scale Characterization of Barium Titanate Powders Formed by the Hydrothermal Process. *J. Am. Ceram. Soc.* **2008**, *91*, 1002–1008.

(33) Zhu, X.; Zhang, Z.; Zhu, J.; Zhou, S.; Liu, Z. Morphology and Atomic-Scale Surface Structure of Barium Titanate Nanocrystals Formed at Hydrothermal Conditions. *J. Cryst. Growth* **2009**, *311*, 2437–2442.

(34) Zhu, X.; Zhu, J.; Zhou, S.; Liu, Z.; Ming, N.; Hesse, D. $BaTiO_3$ Nanocrystals: Hydrothermal Synthesis and Structural Characterization. *J. Cryst. Growth* **2005**, *283*, 553–562.

(35) Elissalde, C.; Chung, U.-C.; Philippot, G.; Lesseur, J.; Berthelot, R.; Sallagoity, D.; Albino, M.; Epherre, R.; Chevallier, G.; Buffière, S.; Weibel, A.; Bernard, D.; Majimel, J.; Aymonier, C.; Mornet, S.; Estournès, C.; Maglione, M. Innovative Architectures in Ferroelectric Multi-Materials: Chemistry, Interfaces and Strain. *J. Adv. Dielectr.* **2015**, *5*, 1530001 1–11.

(36) Philippot, G.; Albino, M.; Epherre, R.; Chevallier, G.; Beynet, Y.; Manière, C.; Weibel, A.; Peigney, A.; Deluca, M.; Elissalde, C.; Maglione, M.; Aymonier, C.; Estournès, C. Local Distortions in Nanostructured Ferroelectric Ceramics through Strain

Tuning. *Adv. Electron. Mater.* **2015**, *1*, 1500190 1–8.

(37) Aoyagi, S.; Kuroiwa, Y.; Sawada, A.; Kawaji, H.; Atake, T. Size Effect on Crystal Structure and Chemical Bonding Nature in $BaTiO_3$ Nanopowder. *J. Therm. Anal. Calorim.* **2005**, *81*, 627–630.

(38) Buscaglia, V.; Buscaglia, M. T.; Viviani, M.; Mitoseriu, L.; Nanni, P.; Trefiletti, V.; Piaggio, P.; Gregora, I.; Ostapchuk, T.; Pokorný, J.; Petzelt, J. Grain Size and Grain Boundary-Related Effects on the Properties of Nanocrystalline Barium Titanate Ceramics. *J. Eur. Ceram. Soc.* **2006**, *26*, 2889–2898.

(39) Fang, C.; Zhou, D.; Gong, S. Core-Shell Structure and Size Effect in Barium Titanate Nanoparticle. *Phys. B Condens. Matter* **2011**, *406*, 1317–1322.

(40) Hornebecq, V.; Huber, C.; Maglione, M.; Antonietti, M.; Elissalde, C. Dielectric Properties of Pure $(BaSr)TiO_3$ and Composites with Different Grain Sizes Ranging from the Nanometer to the Micrometer. *Adv. Funct. Mater.* **2004**, *14*, 899–904.

(41) Hoshina, T. Size Effect of Barium Titanate: Fine Particles and Ceramics. *J. Ceram. Soc. Japan* **2013**, *121*, 156–161.

(42) Hoshina, T.; Takizawa, K.; Li, J.; Kasama, T.; Kakemoto, H.; Tsurumi, T. Domain Size Effect on Dielectric Properties of Barium Titanate Ceramics. *Jpn. J. Appl. Phys.* **2008**, *47*, 7607–7611.

(43) Lin, S.; Lü, T.; Jin, C.; Wang, X. Size Effect on the Dielectric Properties of $BaTiO_3$ Nanoceramics in a Modified Ginsburg-Landau-Devonshire Thermodynamic Theory. *Phys. Rev. B* **2006**, *74*, 134115 1–5.

(44) Yoon, S.; Dornseiffer, J.; Xiong, Y.; Grüner, D.; Shen, Z.; Iwaya, S.; Pithan, C.; Waser, R. Spark Plasma Sintering of Nanocrystalline $BaTiO_3$-Powders: Consolidation Behavior and Dielectric Characteristics. *J. Eur. Ceram. Soc.* **2011**, *31*, 1723–1731.

(45) Croker, D.; Loan, M.; Hodnett, B. K. Kinetics and Mechanisms of the Hydrothermal Crystallization of Calcium Titanate Species. *Cryst. Growth Des.* **2009**, *9*, 2207–2213.

(46) Eckert Jr, J.; Hung-Houston, C.; Gersten, B.; Lencka, M.; Riman, R. Kinetics and Mechanisms of Hydrothermal Synthesis of Barium Titanate. *Journal of the American Ceramic Society*. 1996, 2929–2939.

(47) Kalyani, V.; Vasile, B. S.; Ianculescu, A.; Testino, A.; Carino, A.; Buscaglia, M. T.; Buscaglia, V.; Nanni, P. Hydrothermal Synthesis of $SrTiO_3$: Role of Interfaces. *Cryst. Growth Des.* **2015**, *15*, 5712–5725.

(48) Walton, R. I.; Millange, F.; Smith, R. I.; Hansen, T. C.; O'Hare, D. Real Time Observation of the Hydrothermal Crystallization of Barium Titanate Using *in Situ* Neutron Powder Diffraction. *J. Am. Chem. Soc.* **2001**, *123*, 12547–12555.

(49) Philippot, G.; Jensen, K. M. Ø.; Christensen, M.; Elissalde, C.; Maglione, M.; Iversen, B. B.; Aymonier, C. Coupling *in Situ* Synchrotron Radiation with *Ex Situ* Spectroscopy Characterizations to Study the Formation of $Ba_{1-x}Sr_xTiO_3$ Nanoparticles in Supercritical Fluids. *J. Supercrit. Fluids* **2014**, *87*, 111–117.

(50) Adschiri, T.; Hakuta, Y.; Arai, K. Hydrothermal Synthesis of Metal Oxide Fine Particles at Supercritical Conditions. *Ind. Eng. Chem. Res.* **2000**, *39*, 4901–4907.

(51) Adschiri, T.; Hakuta, Y.; Sue, K.; Arai, K. Hydrothermal Synthesis of Metal Oxide Nanoparticles at Supercritical Conditions. *J. Nanoparticle Res.* **2001**, *3*, 227–235.

(52) Aymonier, C.; Loppinet-Serani, A.; Reverón, H.; Garrabos, Y.; Cansell, F. Review of Supercritical Fluids in Inorganic Materials Science. *J. Supercrit. Fluids* **2006**, *38*, 242–251.

(53) Cansell, F.; Aymonier, C. Design of Functional Nanostructured Materials Using Supercritical Fluids. *J. Supercrit. Fluids* **2009**, *47*, 508–516.

(54) Chevalier, B.; Demourgues, A.; Etourneau, J.; Even, C.; Tressaud, A.; Garrabos, Y.; Pessey, V. Supercritical Fluid Processing: A New Route for Materials Synthesis. *J. Mater. Chem.* **1999**, *9*, 67–75.

(55) Hakuta, Y.; Hayashi, H.; Arai, K. Fine Particle Formation Using Supercritical Fluids. *Curr. Opin. Solid State Mater. Sci.* **2003**, *7*, 341–351.

(56) Hayashi, H.; Hakuta, Y. Hydrothermal Synthesis of Metal Oxide Nanoparticles in Supercritical Water. *Materials (Basel).* **2010**, *3*, 3794–3817.

(57) Hayashi, H.; Noguchi, T.; Islam, N. M.; Hakuta, Y.; Imai, Y.; Ueno, N. Hydrothermal Synthesis of $BaTiO_3$ Nanoparticles Using a Supercritical Continuous Flow Reaction System. *J. Cryst. Growth* **2010**, *312*, 1968–1972.

(58) Reverchon, E.; Adami, R. Nanomaterials and Supercritical Fluids. *J. Supercrit. Fluids* **2006**, *37*, 1–22.

(59) Bøjesen, E. D.; Jensen, K. M. Ø.; Tyrsted, C.; Lock, N.; Christensen, M.; Iversen, B. B. *In Situ* Powder Diffraction Study of the Hydrothermal Synthesis of ZnO Nanoparticles. *Cryst. Growth Des.* **2014**, 14, 2803–2810.

(60) Jensen, K. M. Ø.; Andersen, H. L.; Tyrsted, C.; Bøjesen, E. D.; Dippel, A.-C.; Lock, N.; Billinge, S. J. L.; Iversen, B. B.; Christensen, M. Mechanisms for Iron Oxide Formation under Hydrothermal Conditions: An *in Situ* Total Scattering Study. *ACS Nano* **2014**, *8*, 10704–10714.

(61) Jensen, K. M. Ø.; Christensen, M.; Juhas, P.; Tyrsted, C.; Bøjesen, E. D.; Lock, N.; Billinge, S. J. L.; Iversen, B. B. Revealing the Mechanisms behind SnO_2 Nanoparticle Formation and Growth during Hydrothermal Synthesis: An *In Situ* Total Scattering Study. *J. Am. Chem. Soc. Soc.* **2012**, 134, 6785–6792.

(62) Becker, J.; Bremholm, M.; Tyrsted, C.; Pauw, B.;

Jensen, K. M. Ø.; Eltzholt, J.; Christensen, M.; Iversen, B. B. Experimental Setup for *in Situ* X-Ray SAXS/WAXS/PDF Studies of the Formation and Growth of Nanoparticles in near- and Supercritical Fluids. *J. Appl. Crystallogr.* **2010**, *43*, 729–736.

(63) Tyrsted, C.; Lock, N.; Jensen, K. M. Ø.; Christensen, M.; Bøjesen, E. D.; Emerich, H.; Vaughan, G.; Billinge, S. J. L.; Iversen, B. B. Evolution of Atomic Structure during Nanoparticle Formation. *IUCrJ* **2014**, 1, 165–171.

(64) Saha, D.; Jensen, K. M.; Tyrsted, C.; Bøjesen, E. D.; Mamakhel, A. H.; Dippel, A. C.; Christensen, M.; Iversen, B. B. *In Situ* Total X-Ray Scattering Study of WO_3 Nanoparticle Formation under Hydrothermal Conditions. *Angew. Chemie - Int. Ed.* **2014**, *53*, 3667–3670.

(65) Mi, J. L.; Shen, Y.; Becker, J.; Bremholm, M.; Iversen, B. B. Controlling Allotropism in Ruthenium Nanoparticles: A Pulsed-Flow Supercritical Synthesis and *in Situ* Synchrotron X-Ray Diffraction Study. *J. Phys. Chem. C* **2014**, *118*, 11104–11110.

(66) Cerenius, Y.; Ståhl, K.; Svensson, L. a; Ursby, T.; Oskarsson, A.; Albertsson, J.; Liljas, A. The Crystallography Beamline I711 at MAX II. *J. Synchrotron Radiat.* **2000**, *7*, 203–208.

(67) Bocquet, J. F.; Chhor, K.; Pommier, C. Barium Titanate Powders Synthesis from Solvothermal Reaction and Supercritical Treatment. *Mater. Chem. Phys.* **1999**, *57*, 273–280.

(68) Elissalde, C.; Reverón, H.; Aymonier, C.; Michau, D.; Cansell, F.; Maglione, M. The Ferroelectric Transition Temperature as an Intrinsic Probe for Sintered Nanocrystalline $BaTiO_3$ Synthesized under Supercritical Conditions. *Nanotechnology* **2005**, *16*, 797–802.

(69) Reverón, H.; Elissalde, C.; Aymonier, C.; Bidault, O.; Maglione, M.; Cansell, F. Supercritical Fluid Route for Synthesizing Crystalline Barium Strontium Titanate Nanoparticles. *J. Nanosci. Nanotechnol.* **2005**, *5*, 1741–1744.

(70) Reverón, H.; Aymonier, C.; Loppinet-Serani, A.; Elissalde, C.; Maglione, M.; Cansell, F. Single-Step Synthesis of Well-Crystallized and Pure Barium Titanate Nanoparticles in Supercritical Fluids. *Nanotechnology* **2005**, *16*, 1137–1143.

(71) Reverón, H.; Elissalde, C.; Aymonier, C.; Bousquet, C.; Maglione, M.; Cansell, F. Continuous Supercritical Synthesis and Dielectric Behaviour of the Whole BST Solid Solution. *Nanotechnology* **2006**, *17*, 3527–3532.

(72) Hammersley, A. P.; Svensson, S. O.; Hanfland, M.; Fitch, A. N.; Hausermann, D. Two-Dimensional Detector Software: From Real Detector to Idealised Image or Two-Theta Scan. *High Press. Res.* **1996**, *14*, 235–248.

(73) Rodríguez-Carvajal, J. Recent Advances in Magnetic Structure Determination by Neutron Powder Diffraction + FullProf. *Phys. B Condens. Matter* **1993**, *192*, 55–69.

(74) Thompson, P.; Cox, D. E.; Hastings, J. B. Rietveld Refinement of Debye-Scherrer Synchrotron X-Ray Data from A1203. *J. Appl. Phys.* **1987**, *20*, 79–83.

(75) Langford, J. L.; Wilson, A. J. C. Scherrer after Sixty Years: A Survey and Some New Results in the Determination of Crystallite Size. *J. Appl. Crystallogr.* **1978**, *11*, 102–113.

(76) Warren, B. E. *X-Ray Diffraction*; Dover Publications, Inc., Mineola, N., Ed.; 1990.

(77) Larson, A. C.; Von Dreele, R. B. *General Structure Analysis System (GSAS)*; 2004; Vol. 748.

(78) Stokes, a R.; Wilson, a J. C. The Diffraction of X Rays by Distorted Crystal Aggregates - I. *Proc. Phys. Soc.* **2002**, *56*, 174–181.

(79) Bazaev, A. R.; Abdulagatov, I. M.; Bazaev, E. A.; Abdurashidova, A. (p,v,T,x) Measurements of $\{(1-x)H_2O+xC_2H_5OH\}$ Mixtures in the near-Critical and Supercritical Regions. *J. Chem. Thermodyn.* **2007**, *39*, 385–411.

(80) LaMer, V.; Dinegar, R. Theory, Production and Mechanism of Formation of Monodispersed Hydrosols. *J.* **1950**, *72*, 4847–4854.

(81) Nguyen, T.-D.; Do, T.-O. Size- and Shape-Controlled Synthesis of Monodisperse Metal Oxide and Mixed Oxide Nanocrystals. In *Nanotechnology and Nanomaterials*; Masuda, Y., Ed.; InTech, 2011.

(82) Rodríguez-Carvajal, J. *An Introduction to the Program Fullprof 2000 (Laboratorie Léon Brillouin, CEA-CNRS, Saclay)*; 2001.

(83) Yu, Z.; Ang, C.; Guo, R.; Bhalla, a. S. Piezoelectric and Strain Properties of $Ba(Ti_{1-x}Zr_x)O_3$ Ceramics. *J. Appl. Phys.* **2002**, *92*, 1489–1493.

(84) Stephens, P. W.; P.W., S. Phenomenological Model of Anisotropic Peak Broadening in Powder Diffraction. *J. Appl. Crystallogr.* **1999**, *32*, 281–289.

(85) Lee, H.-W.; Moon, S.; Choi, C.-H.; Kim, D. K. Synthesis and Size Control of Tetragonal Barium Titanate Nanopowders by Facile Solvothermal Method. *J. Am. Ceram. Soc.* **2012**, *95*, 2429–2434.

(86) Zeman, M. C.; Fulton, C. C.; Lucovsky, G.; Nemanich, R. J.; Yang, W.-C. Thermal Stability of TiO_2, ZrO_2, or HfO_2 on Si(100) by Photoelectron Emission Microscopy. *J. Appl. Phys.* **2006**, *99*, 023519.

(87) Andersen, H. L.; Christensen, M. *In Situ* Powder X-Ray Diffraction Study of Magnetic $CoFe_2O_4$ Nanocrystallite Synthesis. *Nanoscale* **2015**, *7*, 3481–3490.

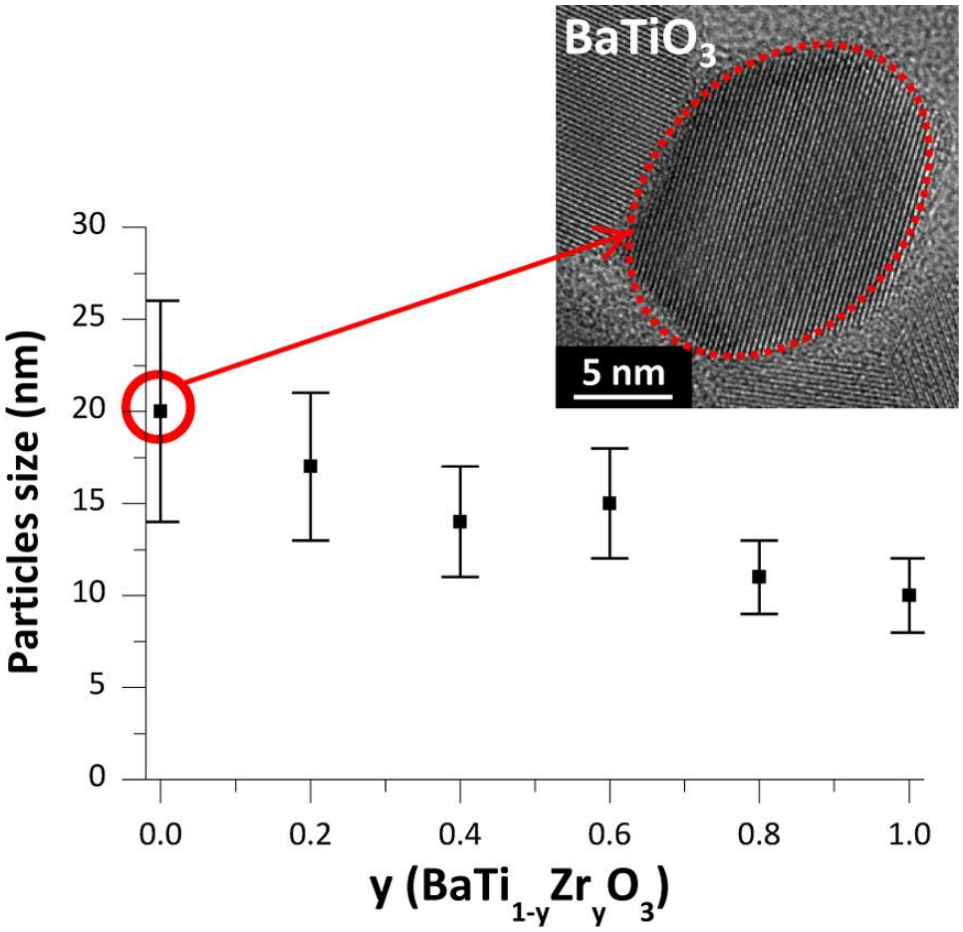

Figure 1. Variation of the BTZ mean nanocrystals size, together with their size distributions, determined from HR-TEM pictures with more than 150 nanocrystals for each composition (see Supporting Information Figure S1 and study by Philippot et al.(24)).

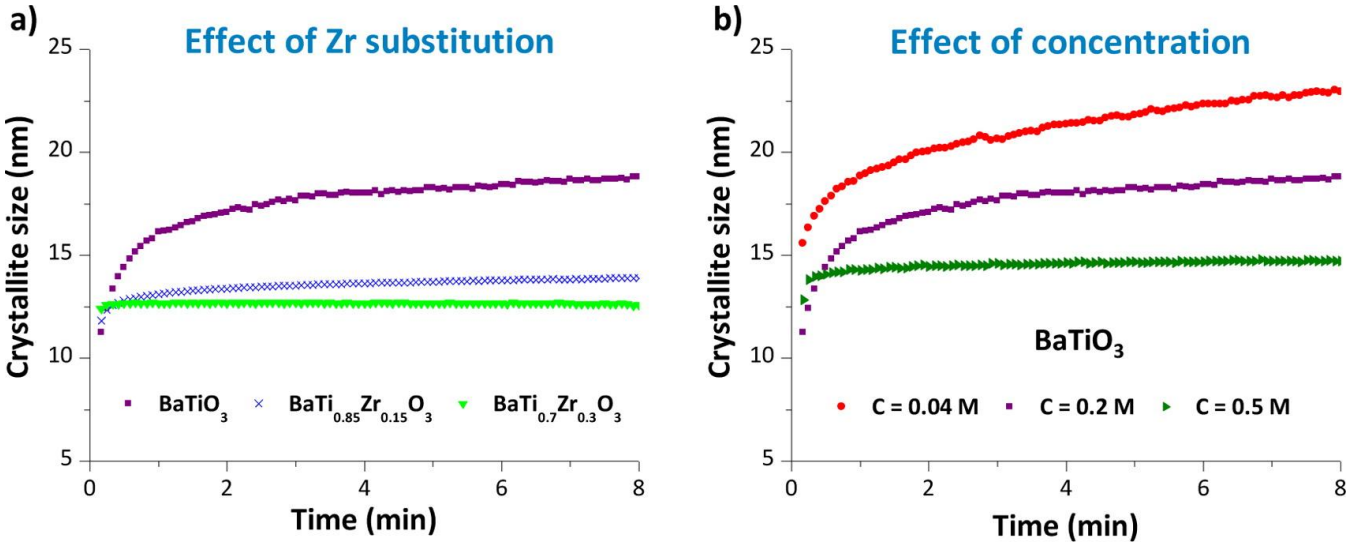

Figure 2. *In situ* synchrotron WAXS study of the BTZ system (a) variation of the crystallite size as a function of time for $BaTiO_3$, $BaTi_{0.85}Zr_{0.15}O_3$, and $BaTi_{0.7}Zr_{0.3}O_3$ and (b) variation of the $BaTiO_3$ crystallite size as a function of time for three different precursor concentrations.

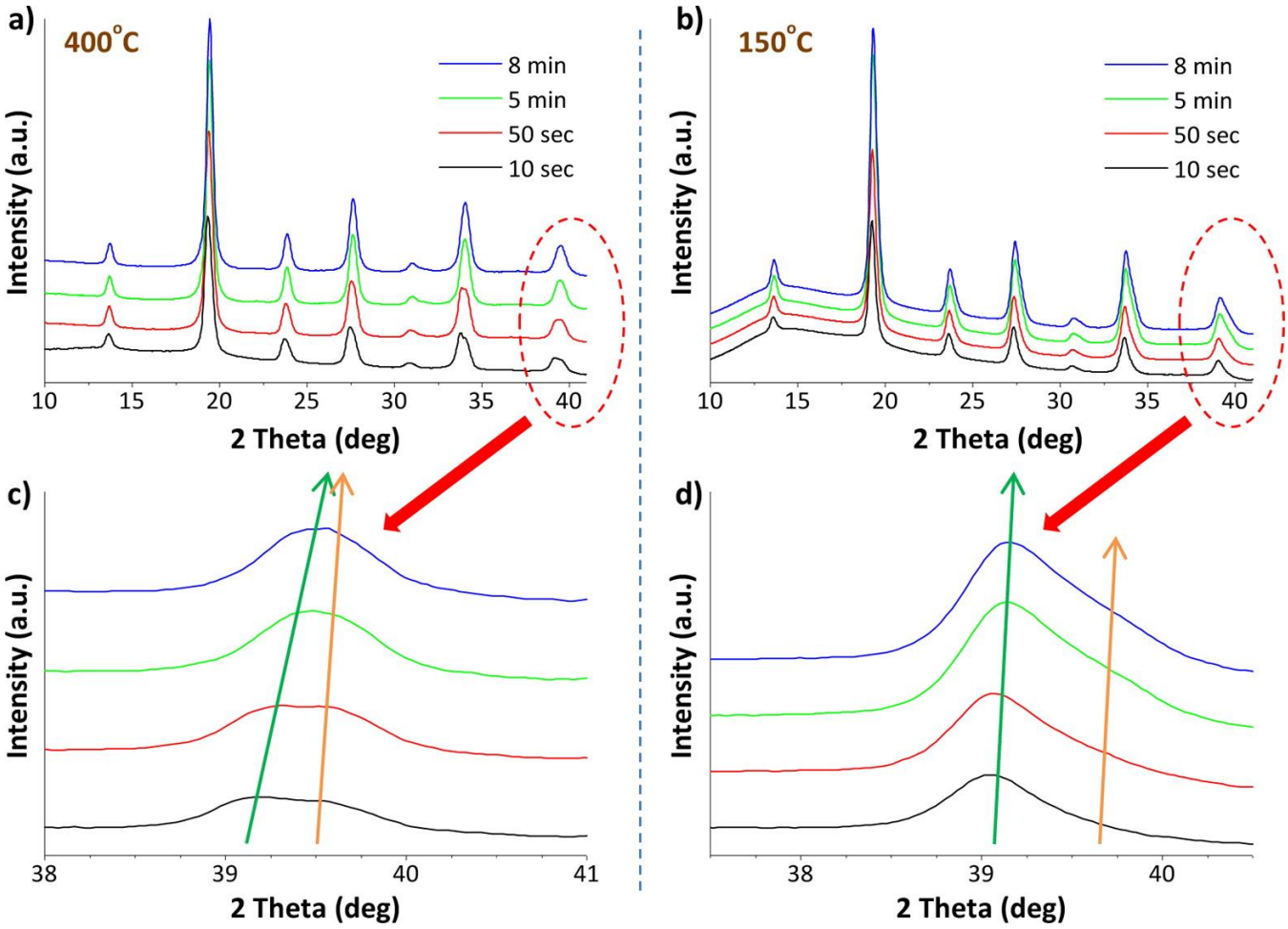

Figure 3. Variation of the WAXS patterns (λ ≈ 0.99361 Å) during the synthesis of $BaTi_{0.4}Zr_{0.6}O_3$ crystallites at different synthesis temperatures: (a) 400 °C with a zoom around 39° (c) and (b) 150 °C with a zoom around 39° (d).

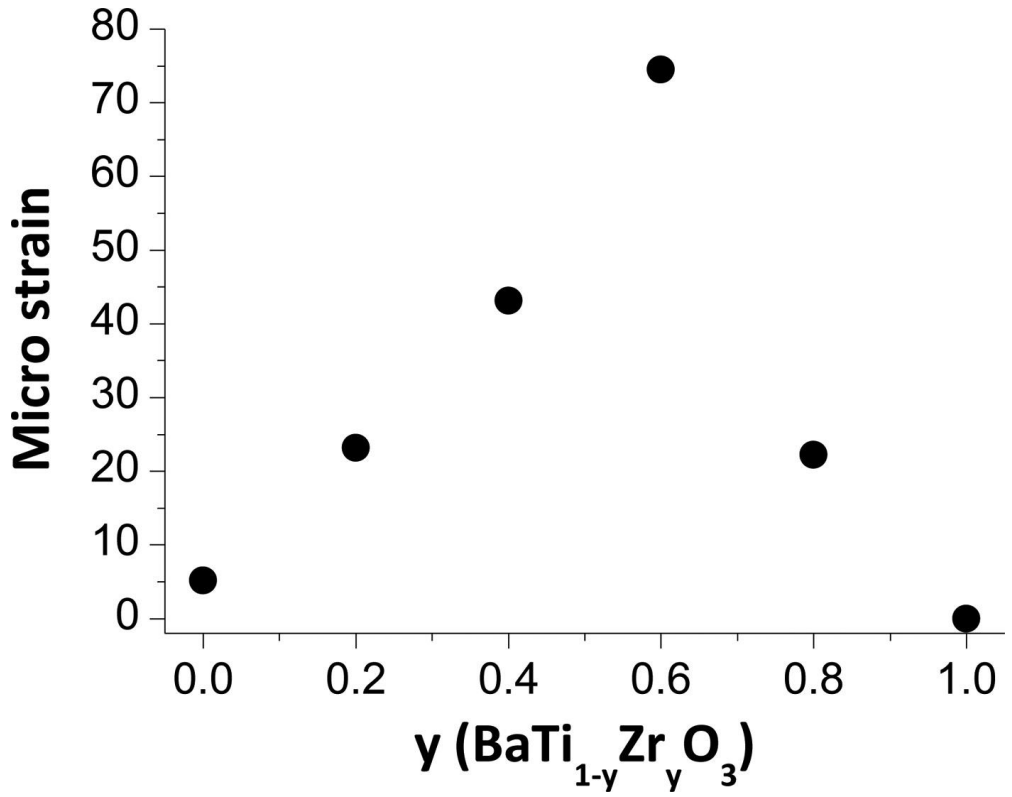

Figure 4. Variation the microstrain parameter with the BTZ composition along the entire solid solution.

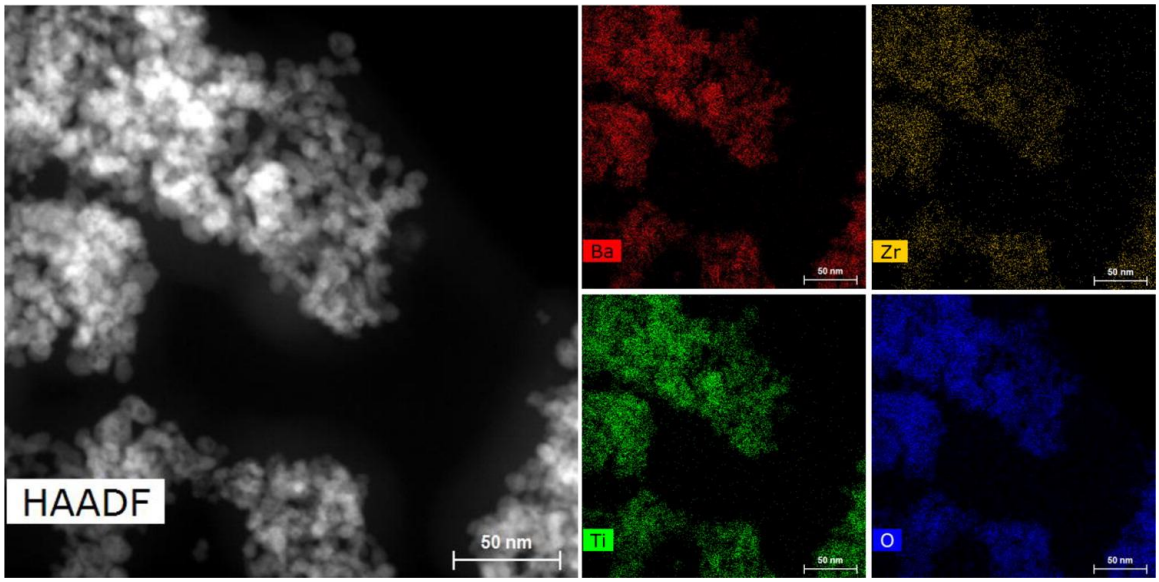

Figure 5. STEM-EDX analysis of the flow synthesized $BaTi_{0.8}Zr_{0.2}O_3$ powder in supercritical conditions (400 °C) confirming a homogeneous distribution of the elements across the particles.

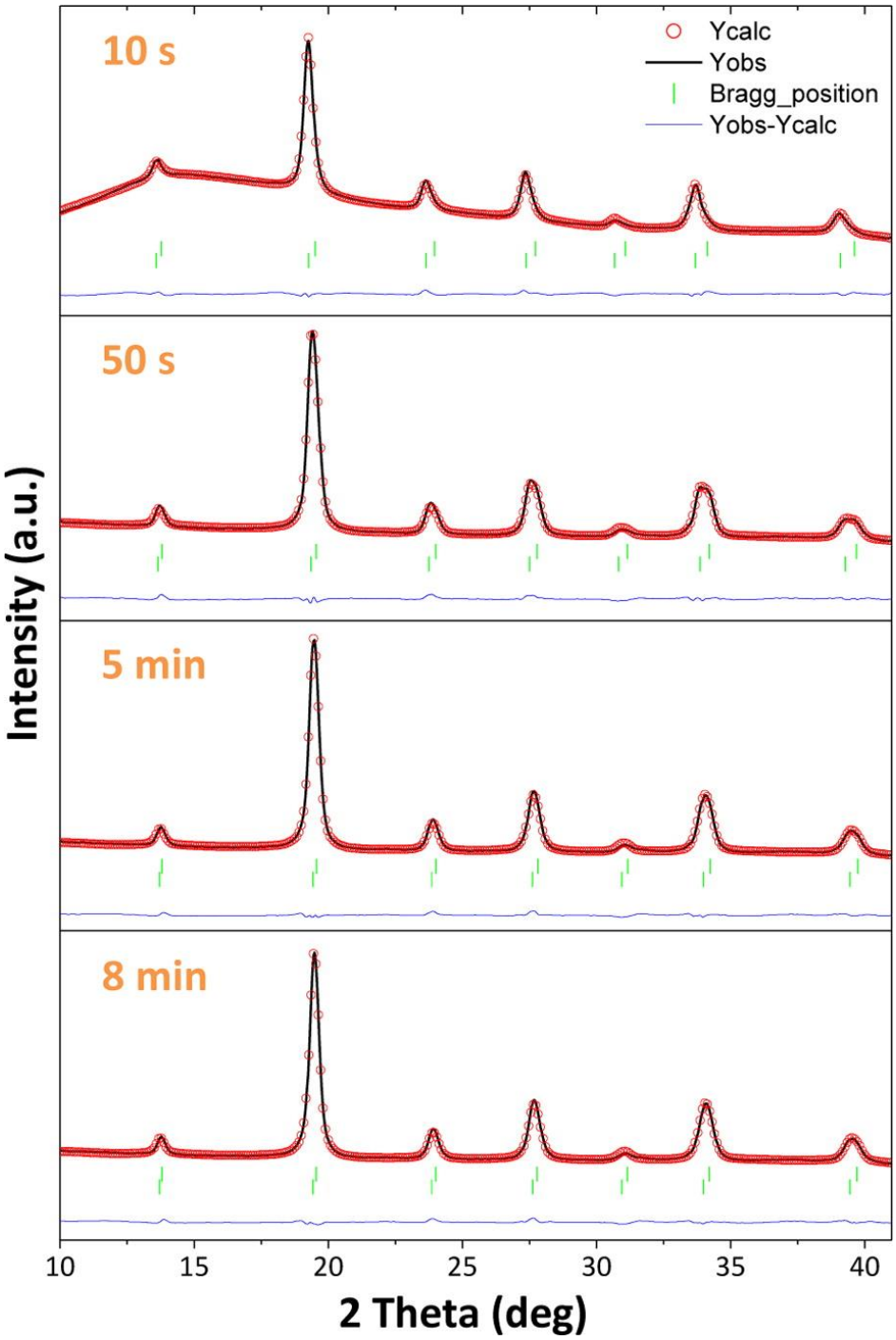

Figure 6. Rietveld refinements fits of the *in situ* XRD data collected for the $BaTi_{0.4}Zr_{0.6}O_3$ system at a synthesis temperature of 400 °C.

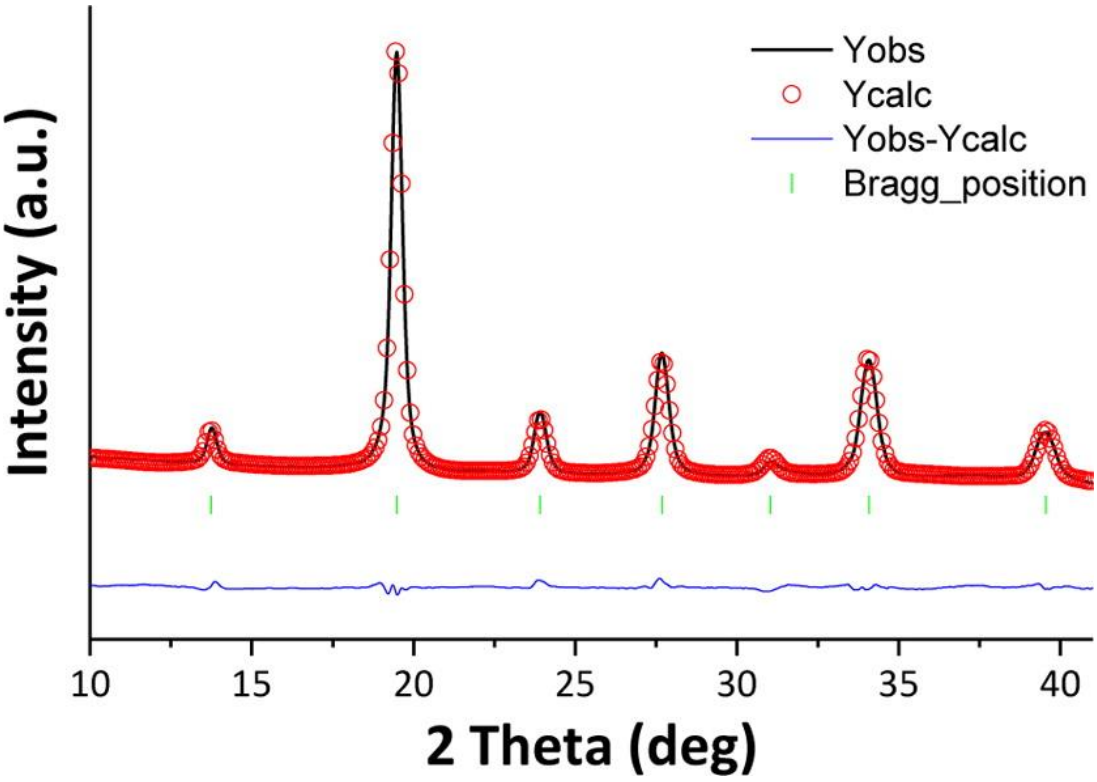

Figure 7. Refinement of the last WAXS pattern corresponding to the $BaTi_{0.4}Zr_{0.6}O_3$ synthesis (after 8 min) with only one group of crystallites but including microstrain.

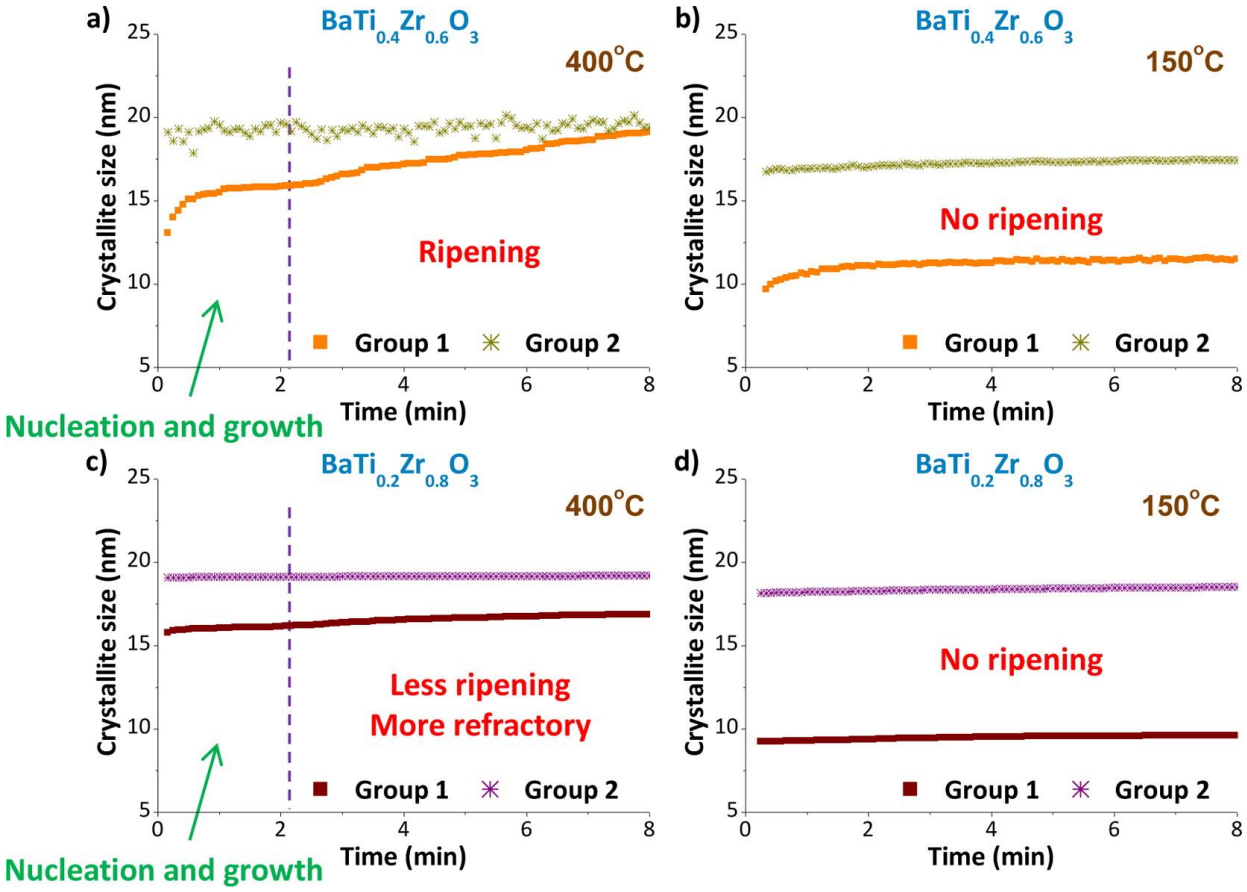

Figure 8. *In situ* study of the crystallite growth in the case of Zr rich phases: (a) $BaTi_{0.4}Zr_{0.6}O_3$ produced at 400 °C, (b) $BaTi_{0.4}Zr_{0.6}O_3$ produced at 150 °C, (c) $BaTi_{0.2}Zr_{0.8}O_3$ produced at 400 °C, and (d) $BaTi_{0.2}Zr_{0.8}O_3$ produced at 150 °C exhibiting two crystallite size populations tending to merge with time only at high temperature (400 °C) and lower Zr content.

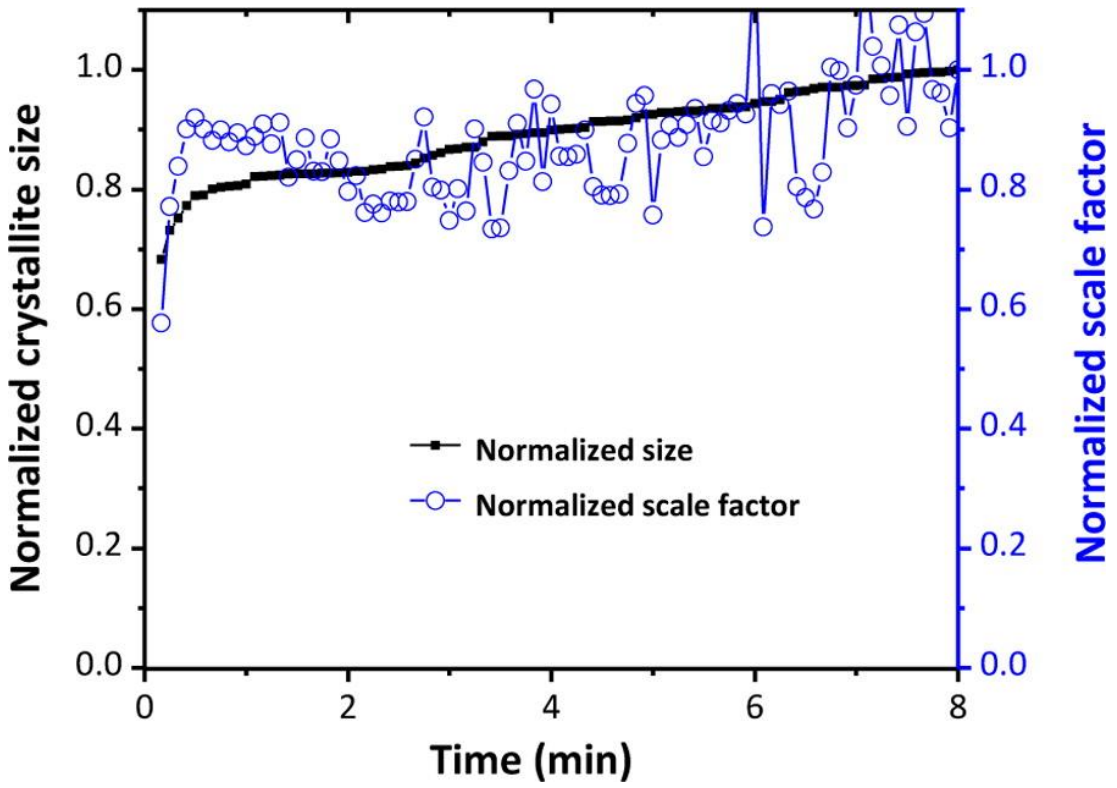

Figure 9. Variation of the normalized scale factor and nanocrystals size according to time for the group 1 of the $BaTi_{0.4}Zr_{0.6}O_3$ synthesis at 400 °C.

Table 1. Comparison of the BTZ Solid Solution XRD Refinements with and without Including a Microstrain Contribution

		compositions y ($BaTi_{1-y}Zr_yO_3$)					
parameters		y = 0	y = 0.2	y = 0.4	y = 0.6	y = 0.8	y = 1
without microstrain	R_B-factor	3.62	3.04	3.80	4.18	1.61	1.07
	R_F-factor	1.64	1.84	2.99	4.80	1.51	1.19
	χ^2	4.75	4.42	2.97	9.77	2.70	2.48
with microstrain	R_B-factor	3.46	3.23	3.08	3.22	1.47	1.08
	R_F-factor	1.53	1.76	1.78	2.17	1.14	1.21
	χ^2	4.64	4.26	2.00	4.57	2.48	2.51